

Inflated nodes and surface states in superconducting half-Heusler compounds

C. Timm,^{1,*} A. P. Schnyder,² D. F. Agterberg,³ and P. M. R. Brydon^{4,†}

¹*Institute of Theoretical Physics, Technische Universität Dresden, 01062 Dresden, Germany*

²*Max-Planck-Institut für Festkörperforschung, Heisenbergstrasse 1, 70569 Stuttgart, Germany*

³*Department of Physics, University of Wisconsin, Milwaukee, Wisconsin 53201, USA*

⁴*Department of Physics, University of Otago, P.O. Box 56, Dunedin 9054, New Zealand*

(Dated: July 17, 2017)

Two topics of high current interest in the field of unconventional superconductivity are noncentrosymmetric superconductors and multiband superconductivity. Half-Heusler superconductors such as YPtBi exemplify both. In this paper, we study bulk and surface states in nodal superconducting phases of the half-Heusler compounds, belonging to the A_1 ($s + p$ -like) and T_2 ($k_z k_x + i k_z k_y$ -like) irreducible representations of the point group. These two phases preserve and break time-reversal symmetry, respectively. For the A_1 case, we find that flat surface bands persist in the multiband system. In addition, the system has dispersive surface bands with zero-energy crossings forming Fermi arcs, which are protected by mirror symmetries. For the T_2 case, there is an interesting coexistence of point and line nodes, known from the single-band case, with Bogoliubov Fermi surfaces (two-dimensional nodes). There are no flat-band surface states, as expected, but dispersive surface bands with Fermi arcs exist. If these arcs do not lie in high-symmetry planes, they are split by the antisymmetric spin-orbit coupling so that their number is doubled compared to the inversion-symmetric case.

I. INTRODUCTION

Topologically nontrivial superconducting states are currently receiving a lot of attention, in part motivated by the vision of topologically protected quantum computation [1]. Several different approaches concern heterostructures in which topological superconductivity is induced at the interface [2–5]. The present paper belongs to another research direction, which focuses on superconductors that are intrinsically topologically nontrivial. For fully gapped superconductors in any number of dimensions, the possible topological states can be classified [6, 7] on the basis of the ten Altland-Zirnbauer symmetry classes [8]. However, many unconventional superconductors do not have a full gap but are nodal, i.e., they feature quasi-particle states at the Fermi energy. It has been realized that such superconductors can also be topologically nontrivial and topological invariants associated with nodes of dimension zero (points), one (lines), and two (surfaces) have been constructed [9–18].

An important class of unconventional superconductors are the noncentrosymmetric materials [19, 20], in which the absence of inversion symmetry allows for the appearance of antisymmetric spin-orbit coupling (ASOC). In single-band systems, due to the ASOC, the spin of a Cooper pair is not a good quantum number, leading to the mixing of (time-reversal-invariant) singlet and triplet pairing. If the triplet component is sufficiently large, the superconducting gap develops line nodes that are topologically protected by an integer (\mathbb{Z}) winding number and are accompanied by flat zero-energy surface bands [11, 12, 14, 15, 21, 22]. Lattice symmetries can induce

additional topological invariants protecting points and lines of zeros of the surface-state dispersion [21, 22].

A particularly promising candidate in this class is the half-Heusler compound YPtBi. Measurements of the upper critical field versus temperature indicate a sizable triplet component [23]. This is consistent with the observed linear temperature dependence of the London penetration depth [24], which is attributed to line nodes. Moreover, tunneling spectra between a normal conductor and superconducting YPtBi show a pronounced, though broadened, zero-bias peak [24], which agrees with expectations for an extended flat zero-energy surface band [11, 12, 14, 15, 21, 22]. This motivates the present study of the surface dispersion of two superconducting states that conventionally are expected to have line nodes. The possible pairing states can be classified according to irreducible representations (irreps) of the crystallographic point group T_d . The two states we consider are a time-reversal-symmetric A_1 , $s + p$ -like pairing state with line nodes [24, 25] and a T_2 , $k_z k_x + i k_z k_y$ -like pairing state that breaks time-reversal symmetry and, in the limit of infinitesimal gaps, has both point and line nodes [25].

The T_2 state with broken time-reversal symmetry is also interesting from the perspective of nodal excitations. In particular, it has been shown that when inversion symmetry is present, this state exhibits topologically protected nodal Bogoliubov Fermi surfaces [16–18], i.e., two-dimensional Fermi surfaces of neutral Bogoliubov quasiparticles. The inversion symmetry is required for the topological protection of these Fermi surfaces [16–18], and their fate is unknown once this protection is removed, as is the case in YPtBi. Here we show that with noncentrosymmetric T_d symmetry, this state exhibits a fascinating coexistence of point nodes, line nodes, and Bogoliubov Fermi surfaces.

Another very interesting aspect of the half-Heusler

* carsten.timm@tu-dresden.de

† philip.brydon@otago.ac.nz

superconductors is their topologically nontrivial normal state. Due to the absence of inversion symmetry in the tetrahedral point group T_d and the resulting ASOC, the degeneracy of energy bands is lifted, except at high-symmetry points in the Brillouin zone. The most relevant band here is the four-component Γ_8 band. Among the large family of half-Heusler compounds, some show band inversion of the Γ_8 and the two-component Γ_6 bands [26, 27]. The Fermi energy for the undoped compounds then lies at the Γ_8 point, assuming there is no accidental band overlap away from the Γ point. The compounds with inverted bands can thus be viewed as semimetals with a quadratic band touching point at the Fermi energy or as zero-gap semiconductors. Due to the inverted bands, topologically protected surface states are expected [28]. Band-structure calculations within density-functional theory (DFT) predict the band inversion to be particularly large in YPtBi and LuPtBi [26, 27]. Bands of dispersive surface states have indeed been observed for YPtBi and LuPtBi using angle-resolved photoemission spectroscopy (ARPES) [28]. Superconductivity occurs both in YPtBi [29] and in LuPtBi [30], with transition temperatures of $T_c = 0.77$ K and $T_c = 1.0$ K, respectively. The irreducible multiband character of these compounds due to the dominant Γ_8 band should have interesting consequences for superconductivity. Some of the authors have recently shown that multiband systems allow for novel pairing states that are impossible for a single band [17, 24, 25].

Nontrivial surface states are characteristic for topological materials and provide the most important route to the experimental verification of the topological state, e.g., through tunneling spectroscopy and ARPES. Since superconducting YPtBi and LuPtBi are promising candidates, it is worthwhile to study their surface states in some detail. Not only should nontrivial superconductivity have signatures in the surface dispersion but also the question arises as to what happens to the surface bands of the normal state. In this paper, we analyze the bulk and surface dispersion of half-Heusler superconductors. For numerical calculations, we take parameters appropriate for YPtBi. As mentioned above, we consider two representative pairing states: a time-reversal-symmetric A_1 pairing state with line nodes [24, 25] and a T_2 pairing state that breaks time-reversal symmetry [25]. Since the bands, including the surface bands, are nondegenerate it makes sense to ask about the spin polarization of the Bloch states. Specifically, we obtain the spin polarization of the surface states for the A_1 state.

The rest of this paper is organized as follows. In Sec. II, we introduce the normal-state tight-binding Hamiltonian for the half-Heusler compounds and then the Bogoliubov-de Gennes Hamiltonian for their superconducting states. We give the Hamiltonians both for the extended system and for slabs with (111) and (100) surfaces. In Sec. III, we present and discuss our results for the bulk and the surface, for the A_1 and T_2 pairing states. Finally, we give a summary and draw conclusions in Sec. IV

II. MODEL

We start by setting up an effective tight-binding model on the fcc lattice, which is the Bravais lattice of the half-Heusler structure. The edge length of the conventional, nonprimitive fcc unit cell is set to 2, the nearest-neighbor separation on the fcc lattice is then $\sqrt{2}$. The four-component electron field of the Γ_8 band is described in terms of an effective angular momentum of $j = 3/2$ [17, 25, 31–35]. This angular momentum is due to the coupling of the electron spins with $l = 1$ p -orbitals of the main-group Z ion in the half-Heusler materials with sum formula XYZ , in the present case Bi. The same model applies to materials with zinc-blende structure. As noted in Ref. [17], it can also be used to formally describe the four-component electronic fields generated by two orbitals and spin 1/2. The mapping between the $j = 3/2$ representation and the orbital-spin representation is given in Ref. [17].

Restricting ourselves to only nearest-neighbor hopping on the fcc lattice, the normal-state Hamiltonian H_N is given as a bilinear form of the four-component spinor operator $c_i = (c_{i,3/2}, c_{i,1/2}, c_{i,-1/2}, c_{i,-3/2})^T$ (T denotes transposition) and its Hermitian conjugate c_i^\dagger . The coefficients are expressed in terms of the standard 4×4 angular-momentum $j = 3/2$ matrices J_x , J_y , and J_z . The specific form in real space is

$$\begin{aligned}
 H_N = & \sum_{ij} c_i^\dagger h_{ij} c_j = -t_1 \sum_{\langle ij \rangle} (c_i^\dagger c_j + \text{H.c.}) \\
 & - t_2 \sum_{\langle ij \rangle} \left(c_i^\dagger J_{\eta_{ij}}^2 c_j + \text{H.c.} \right) \\
 & - t_3 \sum_{\langle ij \rangle} \left(c_i^\dagger \sum_{\nu \neq \nu'} r_{ij,\nu} J_\nu r_{ij,\nu'} J_{\nu'} c_j + \text{H.c.} \right) \\
 & - t_4 \sum_{\langle ij \rangle} (i c_i^\dagger \mathbf{r}_{ij} \cdot \mathbf{K} c_j + \text{H.c.}) \\
 & - t_5 \sum_{\langle ij \rangle} \left[i c_i^\dagger \sum_{\nu} r_{ij,\nu} (r_{ij,\nu+1}^2 - r_{ij,\nu+2}^2) J_\nu c_j + \text{H.c.} \right] \\
 & - \mu \sum_i c_i^\dagger c_i, \tag{1}
 \end{aligned}$$

where $\mathbf{r}_{ij} \equiv \mathbf{R}_i - \mathbf{R}_j$ in terms of the fcc lattice sites \mathbf{R}_i , $\eta_{ij} = x, y$, and z for \mathbf{r}_{ij} perpendicular to the x, y , and z axes, i.e., lying in the yz, zx , and xy planes, respectively, \mathbf{K} is the vector of matrices $K_\nu \equiv J_{\nu+1} J_\nu J_{\nu+1} - J_{\nu+2} J_\nu J_{\nu+2}$, where the notation “ $\nu + 1$ ” and “ $\nu + 2$ ” pertains to the cyclic group $\{x, y, z\}$, and $\sum_{\langle ij \rangle}$ denotes a sum over nearest-neighbor bonds, counting each bond once. This Hamiltonian is compatible with the space group $F43m$ of half-Heusler compounds. The t_4 and t_5 terms represent the ASOC. Our numerical results are obtained for $t_5 = 0$ and we drop the t_5 term from now on. However, all statements on symmetries and topological protection remain valid in the presence of this term.

The superconducting state is described by the second-quantized Hamiltonian

$$H = \frac{1}{2} \sum_{ij} \Psi_i^\dagger \mathcal{H}_{ij} \Psi_j, \quad (2)$$

in terms of the Nambu spinor

$$\Psi_i = \begin{pmatrix} c_i \\ c_i^{\dagger T} \end{pmatrix} \quad (3)$$

and the Bogoliubov-de Gennes Hamiltonian

$$\mathcal{H}_{ij} = \begin{pmatrix} h_{ij} & \Delta_{ij} \\ \Delta_{ji}^\dagger & -h_{ji}^T \end{pmatrix}, \quad (4)$$

where h_{ij} is defined in Eq. (1). In this paper, we are not concerned with the origin of the superconducting pairing. This has recently been considered in Refs. [33, 34, 36].

The effective angular momentum $j = 3/2$ allows for Cooper pairs with total angular momenta $J = 0$ (singlet), $J = 1$ (triplet), $J = 2$ (quintet), $J = 3$ (septet) [25, 31–34]. By subducing the irreps of $O(3)$ of order J to the point group T_d and reducing them into irreps of T_d , one finds the appropriate irreps for any J . In this way, one finds that, for a purely local (s -wave) pairing potential, there must be one singlet pairing state transforming according to the trivial irrep A_1 and five quintet pairing states transforming according to the two-dimensional irrep E and to the three-dimensional irrep T_2 . The on-site pairing Hamiltonian can be written as

$$H_{\text{pair}}^s = \sum_{i,r} \left(\Delta_r^{0*} c_i^T \Gamma_r^\dagger c_i + \Delta_r^0 c_i^\dagger \Gamma_r c_i^{\dagger T} \right), \quad (5)$$

where the index r enumerates the possible local pairing terms, specifying the irrep and also an index counting components for the higher-dimensional irreps. The matrices $\Gamma_r = D_r U_T$ can be written as products of irreducible tensor operators D_r of the appropriate irreps [37–39] and the unitary part

$$U_T = \begin{pmatrix} 0 & 0 & 0 & 1 \\ 0 & 0 & -1 & 0 \\ 0 & 1 & 0 & 0 \\ -1 & 0 & 0 & 0 \end{pmatrix} \quad (6)$$

of the antiunitary time-reversal operator $\mathcal{T} = U_T \mathcal{K}$ (\mathcal{K} is complex conjugation). We hence find the matrices

$$\Gamma_{A_1} = U_T, \quad (7)$$

$$\Gamma_{E,1} = \frac{1}{3} (2J_z^2 - J_x^2 - J_y^2) U_T, \quad (8)$$

$$\Gamma_{E,2} = \frac{1}{\sqrt{3}} (J_x^2 - J_y^2) U_T, \quad (9)$$

$$\Gamma_{T_2,1} = \frac{1}{\sqrt{3}} (J_y J_z + J_z J_y) U_T, \quad (10)$$

$$\Gamma_{T_2,2} = \frac{1}{\sqrt{3}} (J_z J_x + J_x J_z) U_T, \quad (11)$$

$$\Gamma_{T_2,3} = \frac{1}{\sqrt{3}} (J_x J_y + J_y J_x) U_T. \quad (12)$$

Γ_{A_1} belongs to the singlet ($J = 0$) irrep A_1 , whereas the other five belong to the quintet ($J = 2$) irreps E and T_2 . All six matrices are invariant under time reversal. This local pairing enters Δ_{ij} in Eq. (4) as

$$\Delta_{ij}^s = 2\delta_{ij} \sum_r \Delta_r^0 \Gamma_r. \quad (13)$$

A local pairing term that transforms according to a certain irrep will generically be accompanied by nonlocal pairing transforming in the same manner. The best studied example is singlet-triplet mixing in single-band non-centrosymmetric superconductors [14, 15, 21, 22, 40, 41]. Frigeri *et al.* [42] have shown for the single-band case that pair breaking due to the ASOC is avoided for triplet pairing with the same momentum (and hence spatial) dependence as the ASOC. This is thus expected to be the most favorable triplet pairing state.

The natural generalization to the $j = 3/2$ case is the pairing matrix $\Delta_{ij}^p \propto h_{ij}^{\text{ASOC}} U_T$, where h_{ij}^{ASOC} is the ASOC part of h_{ij} . The superscript p stands for p -wave. We thus write

$$\Delta_{ij}^p = -i \Delta_p^0 \mathbf{r}_{ij} \cdot \mathbf{K} U_T, \quad (14)$$

where i and j are nearest-neighbor sites. This pairing term satisfies time-reversal symmetry. By construction, it is also invariant under the lattice symmetries of the normal state. For this reason, it will generically coexist with the local A_1 singlet pairing, which also transforms trivially under the lattice symmetries [25].

The real-space formulation can be used for both extended, bulk system and for slabs of various orientations. We now discuss these two cases in turn.

A. Extended system

For the extended system, we Fourier transform the Hamiltonian in all three directions. The normal-state tight-binding Hamiltonian is then

$$H_N = \sum_{\mathbf{k}} c_{\mathbf{k}}^\dagger h(\mathbf{k}) c_{\mathbf{k}}, \quad (15)$$

where

$$\begin{aligned} h(\mathbf{k}) = & -4t_1 \sum_{\nu} \cos k_{\nu} \cos k_{\nu+1} \\ & - 4t_2 \sum_{\nu} \cos k_{\nu} \cos k_{\nu+1} J_{\nu+2}^2 \\ & + 4t_3 \sum_{\nu} \sin k_{\nu} \sin k_{\nu+1} (J_{\nu} J_{\nu+1} + J_{\nu+1} J_{\nu}) \\ & - 4t_4 \sum_{\nu} \sin k_{\nu} (\cos k_{\nu+1} + \cos k_{\nu+2}) K_{\nu} - \mu \end{aligned} \quad (16)$$

and $c_{\mathbf{k}} = (c_{\mathbf{k},3/2}, c_{\mathbf{k},1/2}, c_{\mathbf{k},-1/2}, c_{\mathbf{k},-3/2})^T$ is the four-component spinor operator. The momentum sum is over

the fcc Brillouin zone. The energy of the Γ_8 band-touching point is $E_0^N = -12t_1 - 15t_2$. The expansion of the coefficients for small \mathbf{k} gives the $\mathbf{k} \cdot \mathbf{p}$ Hamiltonian

$$h_{\mathbf{k}\cdot\mathbf{p}}(\mathbf{k}) = \alpha k^2 + \beta \sum_{\nu} k_{\nu}^2 J_{\nu}^2 + \gamma \sum_{\nu \neq \nu'} k_{\nu} k_{\nu'} J_{\nu} J_{\nu'} + \delta \sum_{\nu} k_{\nu} K_{\nu} - \tilde{\mu}, \quad (17)$$

where $t_1 = \alpha/4 + 15\beta/16$, $t_2 = -\beta/2$, $t_3 = \gamma/4$, $t_4 = -\delta/8$, and $\mu = \tilde{\mu} - 3\alpha - 15\beta/4$. We set $\hbar = 1$ throughout this paper. Identity matrices are suppressed in the first and last terms. This is the $\mathbf{k} \cdot \mathbf{p}$ Hamiltonian used in Ref. [25].

Brydon *et al.* [25] have performed band structure calculations for YPtBi and LuPtBi within DFT, using various approximations for the exchange-correlation functional. The results show significant quantitative differences but agree on the band topology, in particular on the band inversion. The modified Becke-Johnson local-density approximation [43], which was developed to improve the calculated band gaps, predicts stoichiometric YPtBi to be a semimetal with its Fermi energy at the quadratic band-touching point [25].

To be specific, for YPtBi we take the same parameters as in [25], which correspond to $t_1 = -0.918$ eV, $t_2 = 0.760$ eV, $t_3 = -0.253$ eV, and $t_4 = -3.98$ meV. These parameters give reasonable quantitative agreement with the results of the modified Becke-Johnson local-density approximation at small momenta \mathbf{k} and avoids spurious large Fermi surfaces away from the Γ point. Inclusion of the cubic ASOC (t_5) does not significantly improve the agreement. The chemical potential is taken to be $\mu = E_0^N - 0.02$ eV, corresponding to weak hole doping, as seen in experiments [23, 29]. Note that the description of LuPtBi, which has a much more complex normal-state Fermi surface, would require longer-range hoppings in the Hamiltonian.

The four eigenenergies in momentum space are generically nondegenerate. They are strongly split into two pairs by the symmetric t_2 and t_3 terms. In YPtBi, one pair of bands curves up and the other down. The pairs are more weakly split by the antisymmetric t_4 term. All four bands are degenerate at $\mathbf{k} = 0$. This band-touching point is protected by a combination of time-reversal and lattice symmetries: splitting it would require a (mass) term in the Hamiltonian that is independent of \mathbf{k} and not proportional to the identity matrix. One can easily convince oneself that there are only six linearly independent 4×4 matrices that are Hermitian and satisfy time-reversal symmetry. A possible choice for the six matrices is J_x^2 , J_y^2 , J_z^2 , $J_x J_y + J_y J_x$, $J_y J_z + J_z J_y$, and $J_z J_x + J_x J_z$. One can then check that there is no combination except for the identity matrix that also satisfies all symmetries of the point group T_d .

For weak electron or hole doping, the model develops two small, nested Fermi pockets. The pockets have first-order (conical) touching points on the k_x , k_y , and k_z axes,

which are protected by the twofold degeneracy of bands on these axes following from the splitting of the four-dimensional irrep Γ_8 of T_d into two-dimensional irreps $\Delta_5 + \Delta_5$ of C_{2v} .

The superconducting system is described by the Hamiltonian

$$H = \frac{1}{2} \sum_{\mathbf{k}} \Psi_{\mathbf{k}}^{\dagger} \mathcal{H}(\mathbf{k}) \Psi_{\mathbf{k}}, \quad (18)$$

in terms of the Nambu spinor $\Psi_{\mathbf{k}} = (c_{\mathbf{k}}^T, c_{-\mathbf{k}}^{\dagger})^T$, and the Bogoliubov-de Gennes Hamiltonian

$$\mathcal{H}(\mathbf{k}) = \begin{pmatrix} h(\mathbf{k}) & \Delta(\mathbf{k}) \\ \Delta^{\dagger}(\mathbf{k}) & -h^T(-\mathbf{k}) \end{pmatrix}. \quad (19)$$

Here, $h(\mathbf{k})$ is the normal-state Hamiltonian defined in Eq. (16) and the pairing potential is $\Delta(\mathbf{k}) = \Delta^s(\mathbf{k}) + \Delta^p(\mathbf{k})$ with

$$\Delta^s(\mathbf{k}) = 2 \sum_r \Delta_r^0 \Gamma_r, \quad (20)$$

$$\Delta^p(\mathbf{k}) = -4\Delta_p^0 \sum_{\nu} \sin k_{\nu} (\cos k_{\nu+1} + \cos k_{\nu+2}) K_{\nu} U_T. \quad (21)$$

Note that the p -wave gap $\Delta^p(\mathbf{k})$ is only present in the A_1 state.

B. Slabs of finite thickness

In the following section, we will show results of the numerical diagonalization of the Bogoliubov-de Gennes tight-binding model on slabs with (111) and with (100) surface orientations. The thickness W of the slabs has to be chosen large enough to suppress the hybridization of states localized at opposite surfaces. Since the slabs have translation symmetry in the directions parallel to the surfaces, we block diagonalize the Hamiltonian in Eq. (1) by performing a Fourier transformation in these two directions. The corresponding wave vector parallel to the surfaces is denoted by $\mathbf{k}_{\parallel} = (k_1, k_2)$.

We start with a slab with (111) surfaces. The primitive bulk unit cell compatible with the symmetry of the (111) slab is hexagonal and contains three fcc sites. The thickness W is here defined as the number of triangular layers parallel to the surfaces, which means that the unit cell has a height of 3 layers and the slab is $W/3$ hexagonal unit cells thick. The layers are enumerated by $l = 0, \dots, W - 1$. Momentum sums are taken over the two-dimensional Brillouin zone of the slab, which is a hexagon. The components (k_1, k_2) are defined in Fig. 1(a). Special points have the two-dimensional coordinates $K = (2\sqrt{2}\pi/3, 0)$, $K' = (\sqrt{2}\pi/3, \sqrt{2/3}\pi)$, and $M = (0, \sqrt{2/3}\pi)$. In terms of the bulk coordinate sys-

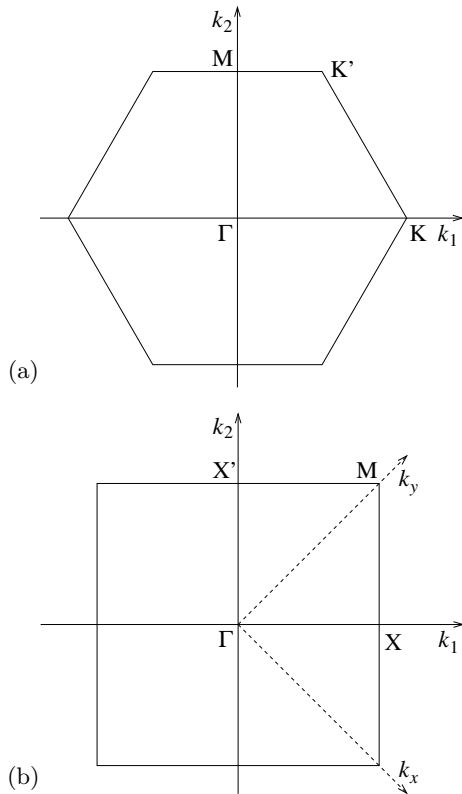


Figure 1. (a) Two-dimensional Brillouin zone of a slab with (a) (111) and (b) (100) surfaces.

tem, the momentum reads

$$\mathbf{k}_{\parallel} = k_1 \frac{1}{\sqrt{2}} \begin{pmatrix} 1 \\ -1 \\ 0 \end{pmatrix} + k_2 \frac{1}{\sqrt{6}} \begin{pmatrix} 1 \\ 1 \\ -2 \end{pmatrix}. \quad (22)$$

The second-quantized Hamiltonian for the slab is

$$H_{\text{slab}} = \frac{1}{2} \sum_{\mathbf{k}_{\parallel}} \sum_{l'l'} \Psi_{\mathbf{k}_{\parallel}l}^{\dagger} \mathcal{H}_{l'l'}^{(111)}(\mathbf{k}_{\parallel}) \Psi_{\mathbf{k}_{\parallel}l'}, \quad (23)$$

with the obvious definition of $\Psi_{\mathbf{k}_{\parallel}l}$ and the matrices

$$\mathcal{H}_{l'l'}^{(111)}(\mathbf{k}_{\parallel}) = \begin{pmatrix} h_{l'l'}^{(111)}(\mathbf{k}_{\parallel}) & \Delta_{l'l'}^{(111)}(\mathbf{k}_{\parallel}) \\ \Delta_{l'l'}^{(111)}(\mathbf{k}_{\parallel})^{\dagger} & -h_{l'l'}^{(111)}(-\mathbf{k}_{\parallel})^T \end{pmatrix}, \quad (24)$$

which can be expressed in terms of 4×4 blocks $h_{l'l'}^{(111)}(\mathbf{k}_{\parallel})$ and $\Delta_{l'l'}^{(111)}(\mathbf{k}_{\parallel})$. The construction of these blocks is a straightforward exercise and their explicit forms are omitted here.

We next consider a slab with (100) surfaces. The (non-primitive) bulk unit cell compatible with the symmetry of this slab is centered tetragonal and contains two sites. The thickness W is defined as the number of square layers parallel to the surfaces, which means that the slab is $W/2$ tetragonal unit cells thick. The layers are again

enumerated by $l = 0, \dots, W - 1$. The momentum vector parallel to the surface is

$$\mathbf{k}_{\parallel} = k_1 \frac{1}{\sqrt{2}} \begin{pmatrix} 0 \\ 1 \\ 1 \end{pmatrix} + k_2 \frac{1}{\sqrt{2}} \begin{pmatrix} 0 \\ -1 \\ 1 \end{pmatrix}. \quad (25)$$

The two-dimensional Brillouin zone of the slab is a square, which is shown in Fig. 1(b). Note that the k_1 and k_2 axes for the slab are rotated by 45° with respect to the conventional cubic axes of the bulk. The two-dimensional coordinates (k_1, k_2) of special points are $M = (\pi/\sqrt{2}, \pi/\sqrt{2})$, $X = (\pi/\sqrt{2}, 0)$, and $X' = (0, \pi/\sqrt{2})$. The Hamiltonian reads

$$H_{\text{slab}} = \frac{1}{2} \sum_{\mathbf{k}_{\parallel}} \sum_{l'l'} \Psi_{\mathbf{k}_{\parallel}l}^{\dagger} \mathcal{H}_{l'l'}^{(100)}(\mathbf{k}_{\parallel}) \Psi_{\mathbf{k}_{\parallel}l'}, \quad (26)$$

with

$$\mathcal{H}_{l'l'}^{(100)}(\mathbf{k}_{\parallel}) = \begin{pmatrix} h_{l'l'}^{(100)}(\mathbf{k}_{\parallel}) & \Delta_{l'l'}^{(100)}(\mathbf{k}_{\parallel}) \\ \Delta_{l'l'}^{(100)}(\mathbf{k}_{\parallel})^{\dagger} & -h_{l'l'}^{(100)}(-\mathbf{k}_{\parallel})^T \end{pmatrix}. \quad (27)$$

To distinguish surface from bulk states, we use the total weight in all bands in the central third of the slab. This quantity shows a large contrast between the two types of states and only weak finite-size effects. For time-reversal-symmetric pairing, we take into account the two states with lowest energy by absolute value since the spectrum is symmetric about the Fermi energy.

III. RESULTS

The model system possesses surface states even in the normal phase. This was already found for related gapless semiconductors by D'yakonov and A. V. Khaetskii [44] and recently within DFT for (Y, Lu)PtBi [28]. It is worth pointing out that the DFT calculations [28] indicate that the dispersion of the surface bands depends on the termination of the surface, an aspect that is missed by our simple tight-binding model. In addition, DFT calculations as well as ARPES [28] show a topological Dirac cone of surface states located *below* the hole-like Γ_8 band. These surface states connect the bulk Γ_8 bands to the Γ_6 bands below and are thus not captured by our Γ_8 -only tight-binding model. That the Dirac cone indeed derives from these bands is shown by Chu *et al.* [45], who use a six-band continuum model containing the Γ_8 and Γ_6 bands.

The presence of surface states derived solely from the Γ_8 band can be understood based on a deformation of the Hamiltonian into a topologically nontrivial one. Such an argument can be used to explain the states localized at zig-zag edges of graphene and also to predict surface states at certain surfaces of iron pnictides [46]. The procedure starts by fixing the wave-vector components \mathbf{k}_{\parallel} parallel to the surface. This produces an effectively one-dimensional model with coordinate l , for which the states

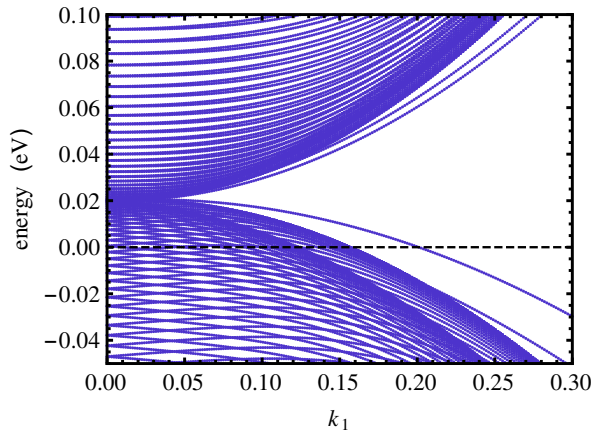


Figure 2. Band structure for the normal state of a slab with (100) surfaces along the k_1 axis. The thickness is $W = 400$. The zero of energy is set to the Fermi energy (dashed horizontal line). The split-off surface bands are clearly visible.

in reciprocal space are enumerated by a wave number k_\perp . We consider wave vectors $\mathbf{k}_\parallel \neq 0$, for which this one-dimensional model is gapped. The corresponding Hamiltonian is then deformed, without closing the gap, into one that has additional symmetries and is topologically nontrivial. We do not give the details here since the manipulations are very similar to Ref. [46]. We end up with two decoupled one-dimensional Hamiltonians in Altland-Zirnbauer class BDI, which allows a \mathbb{Z} topological invariant [6, 7, 16], which in this case turns out to be ± 1 . Hence, the deformed model has two zero-energy surface state per surface, i.e., four in total, for each $\mathbf{k}_\parallel \neq 0$. Now reversing the deformation, the topological protection of these surface states is lost but they evolve continuously as a function of the deformation. Hence, for small deformations, surface states survive but are no longer pinned to zero energy, nor do they remain degenerate. We thus generically expect four surface states at \mathbf{k}_\parallel -dependent energies, i.e., four dispersive surface bands. These surface bands only vanish if the deformation is so large that they become resonant with bulk states.

A cut through the band structure along the positive k_1 axis for a (100) slab in the normal state is plotted in Fig. 2. The plot is restricted to energies close to the Fermi energy and to momenta in the region of the Fermi sea. The quasi-continuous regions correspond to bulk states that are weakly modified by the presence of surfaces. The surface bands are clearly visible in the gap between the bulk bands.

Numerical results for the energy of surface states at (111) and (100) surfaces in the normal phase are shown in Fig. 3. Here and in the following, we only show the central region of the two-dimensional Brillouin zone, in the vicinity of the normal-state Fermi sea. The plot only pertains to the state closest to the Fermi energy for each \mathbf{k}_\parallel . These states are extended through the bulk in the region of the projected Fermi sea (gray in Fig. 3) but

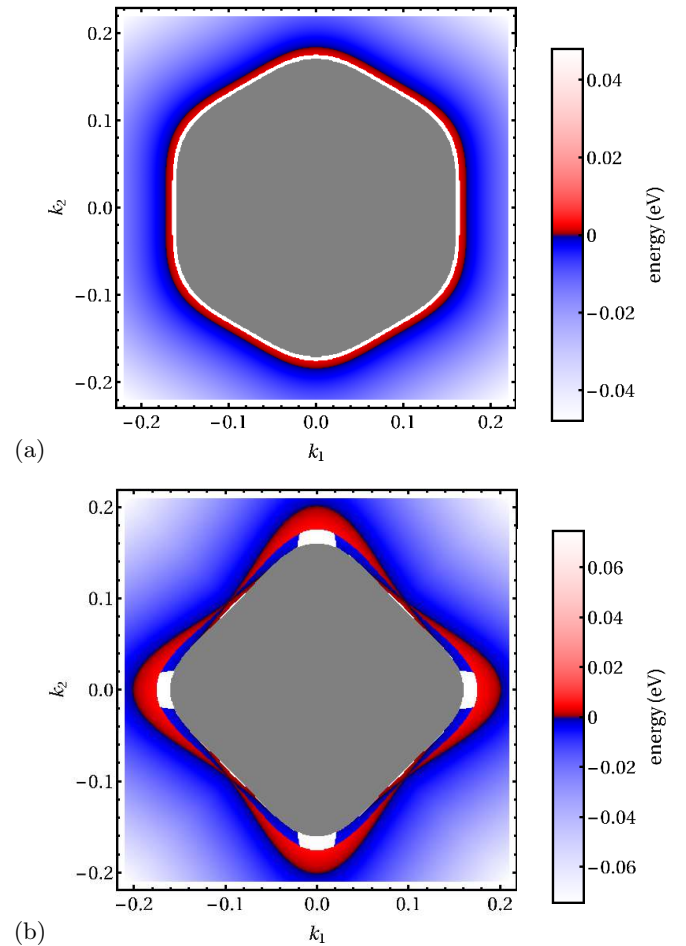


Figure 3. Dispersion of surface states of YPtBi in the normal state for (a) the (111) surface and (b) the (100) surface, for a thickness of $W = 2000$. The gray region in the center is the projection of the bulk Fermi sea, i.e., in this region the states at the Fermi energy are bulk like. Note that this does not preclude the presence of surface states away from the Fermi energy. In the white regions, there is no bulk Fermi sea but the states closest to the Fermi energy are still bulk like.

also in small regions outside of this projection (white). The color denotes the energy of the surface state closest to the Fermi energy. These correspond to the surface bands found by ARPES [28] and also seen in Fig. 2. In agreement with the ARPES experiments and DFT calculations [28], the surface bands cross the Fermi energy from positive to negative values for increasing momentum $\mathbf{k}_\parallel = (k_1, k_2)$. In Fig. 3, this is indicated by a smooth change of color from red through black to blue.

The additional abrupt change of color seen for the (100) surface in Fig. 3(b) is an artifact of the presentation: here, two surface bands have energies of the same absolute value but opposite sign. The white regions in Fig. 3(b) are not a finite-size effect. Figure 2 shows clearly what is happening here: the surface bands continue but the states closest to the Fermi energy are

now bulk like. At smaller momentum, the continuum of bulk states reaches the Fermi energy, corresponding to the gray region in Fig. 3, but the surface bands still continue and approach the quadratic band-touching point.

A. A_1 pairing: flat-band surface states and mirror Fermi arcs

For the superconducting state, we first consider the A_1 gap matrix, in real space,

$$\Delta_{ij} = 2\delta_{ij}\Delta_{A_1}^0\Gamma_{A_1} - i\delta_{\langle ij \rangle}\Delta_p^0\mathbf{r}_{ij}\cdot\mathbf{K}U_T, \quad (28)$$

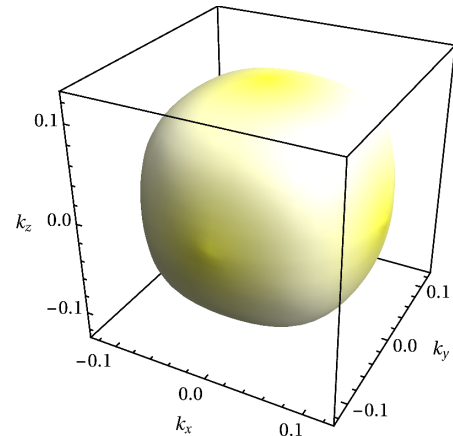
where $\delta_{\langle ij \rangle}$ is unity (zero) if i and j are (not) nearest-neighbor sides. The amplitudes $\Delta_{A_1}^0$ and Δ_p^0 are both taken to be real. As noted above, both terms have the same, namely trivial, transformation properties under all lattice symmetries and thus generically coexist [25]. The state also preserves time-reversal symmetry. The superconducting gap has line nodes when $\Delta_p^0/\Delta_{A_1}^0$ is sufficiently large. We take $\Delta_{A_1}^0 = 3$ meV and $\Delta_p^0 = 7$ meV, which leads to six closed line nodes on the larger Fermi surface, surrounding the bulk cubic axes [25]. The smaller Fermi surface is fully gapped. Inverting the sign of $\Delta_{A_1}^0$ or Δ_p^0 moves the nodes to the smaller Fermi surface. Figure 4 shows the absolute value of the gap on the normal-state Fermi surfaces for infinitesimal pairing amplitudes with the same p -wave-to- s -wave ratio $\Delta_p^0/\Delta_{A_1}^0 = 7/3$. The gap is obtained by treating the pairing in first-order perturbation theory. Infinitesimal amplitudes are used here for illustration since for larger amplitudes the energy minima and in particular the nodal rings move away from the normal-state Fermi surfaces. However, the six nodal rings persist for the larger amplitudes used in the following.

Figure 5 shows the dispersion of surface states at the (111) and (100) surfaces. Outside of the projection of the normal-state Fermi surface, we find weakly modified descendants of the normal surface states shown in Fig. 3. Figure 5(b) shows that the surface bands are mostly gapped out by superconducting pairing. However, there are eight symmetry-related points where the gap closes. For the (111) surface, Fig. 5(a), the projections of the six nodal rings are clearly visible as overlapping ellipses. For \mathbf{k}_{\parallel} points within the projection of a single nodal ring, we observe nondegenerate flat bands. These are reminiscent of the flat bands predicted for spin-1/2 noncentrosymmetric nodal superconductors [11, 12, 14, 15, 21, 22, 47, 48]. They indeed have the same origin: The model Hamiltonian is invariant under time reversal and charge conjugation and thus also under their product, i.e., chiral symmetry, which acts as

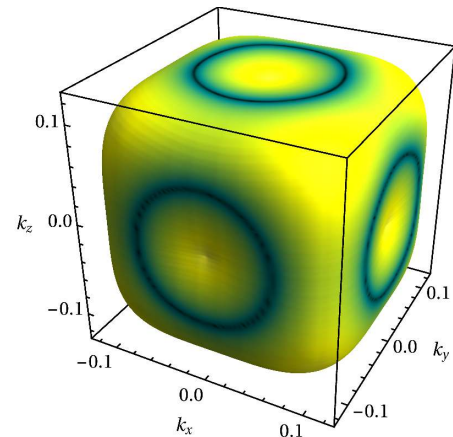
$$S\mathcal{H}(\mathbf{k})S^\dagger = -\mathcal{H}(\mathbf{k}), \quad (29)$$

where the unitary matrix S reads

$$S = \begin{pmatrix} 0 & U_T \\ U_T & 0 \end{pmatrix}. \quad (30)$$



(a)



(b)

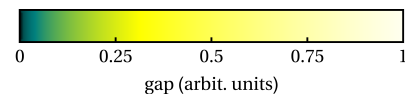


Figure 4. Superconducting gap for the A_1 pairing state with p -wave to s -wave ratio $\Delta_p^0/\Delta_{A_1}^0 = 7/3$ on (a) the smaller and (b) the larger normal-state Fermi surface. Infinitesimal pairing amplitudes have been used for reasons explained in the text.

Let U_S be a unitary matrix that diagonalizes the chiral operator S so that

$$U_S S U_S^\dagger = \begin{pmatrix} i\mathbb{1}_4 & 0 \\ 0 & -i\mathbb{1}_4 \end{pmatrix}, \quad (31)$$

where $\mathbb{1}_4$ is the 4×4 identity matrix. U_S transforms the Hamiltonian into block-off-diagonal form,

$$U_S \mathcal{H}(\mathbf{k}) U_S^\dagger = \begin{pmatrix} 0 & D(\mathbf{k}) \\ D^\dagger(\mathbf{k}) & 0 \end{pmatrix}. \quad (32)$$

For any \mathbf{k}_{\parallel} for which $\det D(\mathbf{k}) \neq 0$ for all k_{\perp} , i.e., any \mathbf{k}_{\parallel} not on a projected node, we can define the winding number

$$W(\mathbf{k}_{\parallel}) = \frac{1}{2\pi} \text{Im} \int dk_{\perp} \frac{\partial}{\partial k_{\perp}} \ln \det D(\mathbf{k}), \quad (33)$$

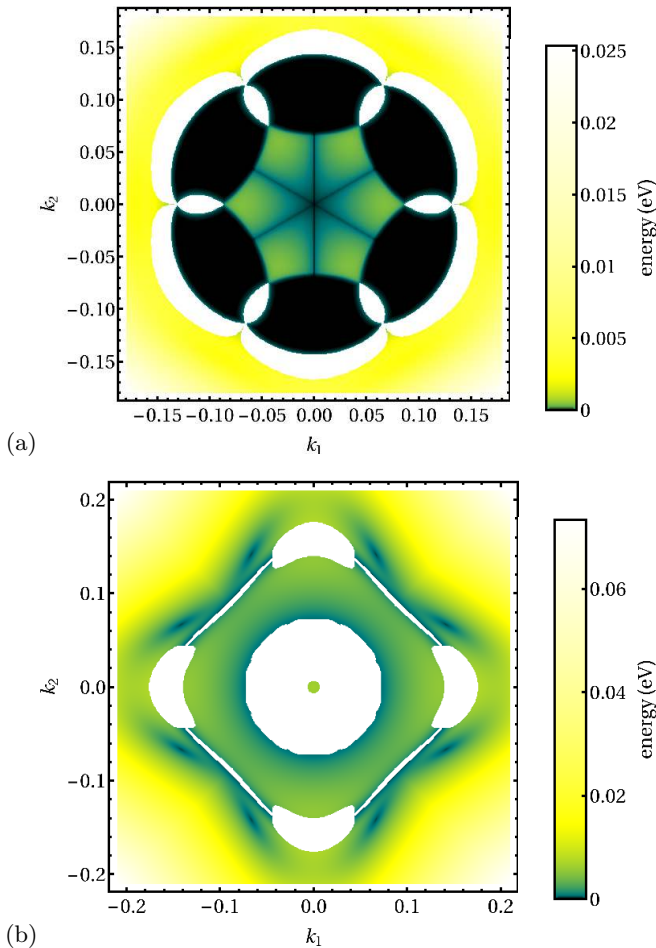


Figure 5. Dispersion of surface states of YPtBi in the superconducting A_1 state for (a) the (111) surface and (b) the (100) surface, for a thickness of $W = 4000$. At each momentum, the states occur in pairs with energies differing in their sign. The positive energy is plotted. Black regions correspond to flat surface bands. In the white regions, the states closest to the Fermi energy are bulk like.

where the integral is over the direction perpendicular to the \mathbf{k}_{\parallel} plane and

$$\mathbf{k} = \mathbf{k}_{\parallel} + k_{\perp} \frac{1}{\sqrt{3}} \begin{pmatrix} 1 \\ 1 \\ 1 \end{pmatrix}. \quad (34)$$

Continuity of the function $\mathbf{k} \mapsto D(\mathbf{k})$ and the properties of the branch point of the logarithm imply that $W(\mathbf{k}_{\parallel}) \in \mathbb{Z}$. For our model, $W(\mathbf{k}_{\parallel}) = \pm 1$ for \mathbf{k}_{\parallel} within the projection of a single nodal ring and $W(\mathbf{k}_{\parallel}) = 0$ otherwise. We indeed find nondegenerate flat bands in exactly these regions. In the limit of infinite thickness, these surface states are at zero energy. They then formally become twofold degenerate but this is just due to the double counting of states in the Nambu formalism. One can interpret them as a pair of Majorana states for each \mathbf{k}_{\parallel} , which are localized at opposite surfaces. In the

regions where the projected nodal rings overlap, there are no flat-band surface states. Here, winding numbers $+1$ and -1 from the two rings add up to zero and the effective one-dimensional system is trivial.

For the (100) surface, Fig. 5(b), four of the nodal rings are viewed edge on and therefore do not lead to flat surface bands. The other two are projected on top of each other. The winding numbers ± 1 from these two nodal rings add up to zero, and so the argument used for the (111) surface does not predict zero-energy flat bands. In agreement with this, we do not find flat bands in this region and in fact also no dispersive surface bands. The small green circle in the center of Fig. 5(b) is likely a finite-size effect; the spectrum here does not show a split-off band.

Furthermore, there are dispersive surface bands for small \mathbf{k}_{\parallel} , where the normal-state Fermi surface has been gapped out. For the (111) surface, Fig. 5(a), their energy goes to zero along lines (“arcs”) connecting the Γ point with the flat bands. These arcs are *not* of the same origin as the ones predicted for noncentrosymmetric superconductors with C_{4v} symmetry in Refs. [14, 21], which result from a \mathbb{Z}_2 invariant protected by an additional time-reversal-like symmetry in two-dimensional planes in momentum space. Instead, they rely on the presence of mirror symmetries. Of the six mirror planes in T_d , the three defined by the equations $k_x - k_y = 0$, $k_y - k_z = 0$, and $k_z - k_x = 0$ are perpendicular to the (111) plane, i.e., the \mathbf{k}_{\parallel} plane, and thus their projections are straight lines. We observe that the arcs form parts of these lines. For example, the mirror symmetry with respect to the $(1\bar{1}0)$ plane with $k_x - k_y = 0$ is expressed as

$$M \mathcal{H}(k_y, k_x, k_z) M^\dagger = \mathcal{H}(k_x, k_y, k_z), \quad (35)$$

with the unitary matrix

$$M = \begin{pmatrix} e^{-i\pi(J_x - J_y)/\sqrt{2}} & 0 \\ 0 & (e^{-i\pi(J_x - J_y)/\sqrt{2}})^* \end{pmatrix} = \begin{pmatrix} e^{-i\pi(J_x - J_y)/\sqrt{2}} & 0 \\ 0 & e^{i\pi(J_x + J_y)/\sqrt{2}} \end{pmatrix}. \quad (36)$$

The $(1\bar{1}0)$ plane corresponds to $k_1 = 0$, i.e., the k_2 axis in Fig. 5(a), while k_2 and k_{\perp} do not change under this reflection. Hence, we can write

$$M \mathcal{H}(k_1 = 0, k_2, k_{\perp}) M^\dagger = \mathcal{H}(k_1 = 0, k_2, k_{\perp}). \quad (37)$$

This is now a symmetry at a single \mathbf{k} point, not one connecting two points. Let U_M be a unitary matrix that diagonalizes M in such a way that

$$U_M M U_M^\dagger = \begin{pmatrix} i\mathbb{1}_4 & 0 \\ 0 & -i\mathbb{1}_4 \end{pmatrix}. \quad (38)$$

Applying this transformation to the Hamiltonian on the

mirror plane makes it block diagonal,

$$U_M \mathcal{H}(0, k_2, k_\perp) U_M^\dagger = \begin{pmatrix} \mathcal{H}_+(k_2, k_\perp) & 0 \\ 0 & \mathcal{H}_-(k_2, k_\perp) \end{pmatrix}, \quad (39)$$

where $\mathcal{H}_+(k_2, k_\perp)$ [$\mathcal{H}_-(k_2, k_\perp)$] is the Bogoliubov-de Gennes Hamiltonian in the sector with mirror eigenvalue i ($-i$). The chiral operator is also invariant under reflection and is block diagonalized by the same transformation,

$$U_M S U_M^\dagger = \begin{pmatrix} \tilde{S} & 0 \\ 0 & -\tilde{S} \end{pmatrix}. \quad (40)$$

Note that the diagonal blocks are identical up to an irrelevant sign. The blocks $\mathcal{H}_\pm(k_2, k_\perp)$ possess chiral symmetry with respect to \tilde{S} :

$$\tilde{S} \mathcal{H}_\pm(k_2, k_\perp) \tilde{S}^\dagger = -\mathcal{H}_\pm(k_2, k_\perp). \quad (41)$$

With the 4×4 unitary matrix $U_{\tilde{S}}$ that diagonalizes \tilde{S} , we can now separately transform the Hamiltonians $\mathcal{H}_\pm(k_2, k_\perp)$ in the two mirror-parity sectors into block-off-diagonal form,

$$U_{\tilde{S}} \mathcal{H}_\pm(k_2, k_\perp) U_{\tilde{S}}^\dagger = \begin{pmatrix} 0 & D_\pm(k_2, k_\perp) \\ D_\pm^\dagger(k_2, k_\perp) & 0 \end{pmatrix}. \quad (42)$$

The winding number in Eq. (33) can also be written as

$$W(\mathbf{k}_\parallel) = -\frac{1}{4\pi i} \int dk_\perp \text{Tr} S \mathcal{H}(\mathbf{k})^{-1} \frac{\partial}{\partial k_\perp} \mathcal{H}(\mathbf{k}). \quad (43)$$

We now rewrite this winding number on the mirror plane, suppressing the arguments (k_2, k_\perp) of \mathcal{H}_\pm ,

$$\begin{aligned} W(k_2) &= -\frac{1}{4\pi i} \int dk_\perp \text{Tr} \left\{ \begin{pmatrix} \tilde{S} \mathcal{H}_+^{-1} & 0 \\ 0 & -\tilde{S} \mathcal{H}_-^{-1} \end{pmatrix} \right. \\ &\quad \left. \times \frac{\partial}{\partial k_\perp} \begin{pmatrix} \mathcal{H}_+ & 0 \\ 0 & \mathcal{H}_- \end{pmatrix} \right\} \\ &= W_+(k_2) - W_-(k_2), \end{aligned} \quad (44)$$

with

$$\begin{aligned} W_\pm(k_2) &\equiv -\frac{1}{4\pi i} \int dk_\perp \text{Tr} \tilde{S} \mathcal{H}_\pm^{-1} \frac{\partial}{\partial k_\perp} \mathcal{H}_\pm \\ &= \frac{1}{2\pi} \text{Im} \int dk_\perp \frac{\partial}{\partial k_\perp} \ln \det D_\pm(k_2, k_\perp). \end{aligned} \quad (45)$$

We find that $W_+(k_2) = W_-(k_2) = -1$ on the arcs. Here, the normal winding number is $W(\mathbf{k}_\parallel) = -1 + 1 = 0$ but the two nontrivial mirror winding numbers $W_\pm(k_2) = -1$ leads to two zero-energy states. The arcs are indeed twofold degenerate if the double counting introduced by the Nambu formalism is corrected for: two pairs of helical Majorana bands cross at $k_1 = 0$. The splitting between the Majorana bands is due to the ASOC. In the flat-band regions, one of $W_\pm(k_2)$ equals -1 and the other vanishes, leading to $W(\mathbf{k}_\parallel) = \pm 1$, as discussed above.

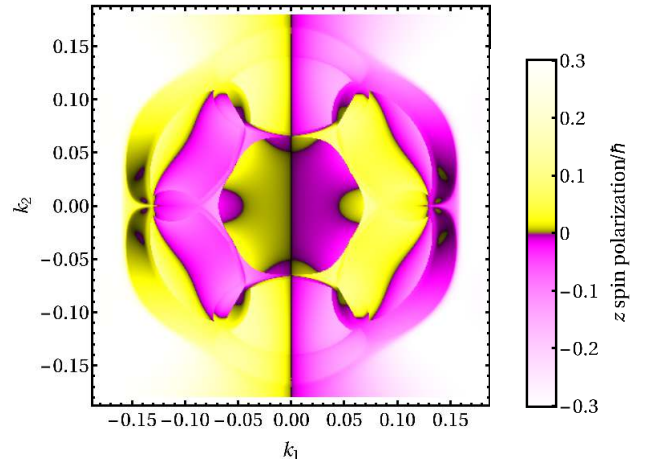


Figure 6. Spin polarization in the z direction, $\langle S_z \rangle = \langle J_z / 3 \rangle$ versus surface momentum \mathbf{k}_\parallel of the lowest-energy state for a (111) slab with $W = 4000$ of YPtBi in the A_1 state. At each momentum, the spectrum is symmetric. For states of nonzero energy, the negative-energy state is used, whereas for degenerate zero-energy states, the superposition localized at the $l = 0$ surface is used.

For larger k_2 , outside of the flat-band regions, we find $W_+(k_2) = W_-(k_2) = 0$ and there is no arc.

The surface states are nondegenerate, except at the arcs. In particular, the flat bands are nondegenerate, as noted above. Therefore, the states are spin polarized and the absolute value of the spin polarization is $1/2$. Physically, the spin polarization of states results from the ASOC. For the single-band case and various point groups, the spin polarization has been calculated in Ref. [49]. In the present case, we have to distinguish between the effective spin \mathbf{J} of length $3/2$ and the electronic spin \mathbf{S} of length $1/2$. In the half-Heusler compounds, the total angular momentum \mathbf{J} results from the combination of the electronic spin \mathbf{S} with an orbital angular momentum \mathbf{L} of length 1 . The spin operators are then obtained by projecting $S_\nu \otimes \mathbb{1}_3$, $\nu = x, y, z$ onto the subspace of total angular momentum $3/2$ [50, 51]. This simply gives $\mathbf{S} = \mathbf{J}/3$ [52].

We show the z component of the spin polarization $\langle \mathbf{S} \rangle$ at the (111) surface in Fig. 6. Making use of the threefold rotation symmetry of the slab with respect to the (111) direction, which is perpendicular to the $\mathbf{k}_\parallel = (k_1, k_2)$ plane, the x and y components can be obtained by rotating the plot by $\pm 120^\circ$ (not shown). Moreover, the mirror planes perpendicular to the surface are visible in the plot. For example, the mirror symmetry of the Bogoliubov-de Gennes Hamiltonian with respect to the $(1\bar{1}0)$ plane is expressed by Eq. (35). In the mirror plane that intersects the \mathbf{k}_\parallel plane along the k_2 axis this relation turns into the invariance (37) at fixed momentum. The same transformation also leaves the spin component $(J_x - J_y)/\sqrt{2}$ invariant. The surface states must therefore be eigenstates of $(J_x - J_y)/\sqrt{2}$. Noting that the components J_z

and $(J_x + J_y)/\sqrt{2}$ are orthogonal to $(J_x - J_y)/\sqrt{2}$, it is elementary to show that the operators J_z and $(J_x + J_y)/\sqrt{2}$ have vanishing diagonal matrix elements in an eigenbasis of $(J_x - J_y)/\sqrt{2}$ so that $\langle J_z \rangle = 0$ and $\langle J_x \rangle = -\langle J_y \rangle$.

B. T_2 pairing: inflated bulk nodes and Chern Fermi arcs

For the half-Heusler compounds, time-reversal-symmetry-breaking states are realized by forming linear combinations of the pairing matrices Γ_r in Eqs. (8)–(12) belonging to the same irrep, with complex coefficients. We here focus on the pairing states belonging to the three-dimensional irrep T_2 . They are characterized by the gap matrix

$$\Delta_{ij} = 2\delta_{ij} \Delta_{T_2}^0 (l_1 \Gamma_{T_2,1} + l_2 \Gamma_{T_2,2} + l_3 \Gamma_{T_2,3}) \quad (46)$$

in terms of the complex three-component order parameter $\mathbf{l} = (l_1, l_2, l_3)$. A free-energy expansion [53] shows that the possible equilibrium states are $\mathbf{l} = (1, 0, 0)$, $(1, 1, 1)$, $(1, e^{2\pi i/3}, e^{4\pi i/3})$, $(1, i, 0)$, and states related to these by point-group operations. The third and fourth state in the list break time-reversal symmetry because of the complex phase factors. For weak pairing, one of these states has the lowest free energy of all T_2 pairing states [25]. As a representative of pairing that breaks time-reversal symmetry, we examine the state with $\mathbf{l} = (1, i, 0)$, i.e.,

$$\Delta_{ij} = 2\delta_{ij} \Delta_{T_2}^0 (\Gamma_{T_2,1} + i \Gamma_{T_2,2}). \quad (47)$$

1. Bulk nodal structure

In the centrosymmetric limit, where the ASOC vanishes, and for infinitesimal pairing amplitude $\Delta_{T_2}^0$, the superconducting gap has both point and line nodes [25]. The point nodes are located at the intersections of the k_z axis with the Fermi surfaces, which have first-order touching points at these intersections. The line nodes exist at the intersections of the $k_x k_y$ plane with both Fermi surfaces. The same nodal structure is found also for stronger pairing if the pairing is purely intraband. Point nodes are not surprising since the superconductor belongs to class D [8], for which point nodes away from high-symmetry points are protected by a \mathbb{Z} topological invariant [16, 22, 54]. The invariant is a first Chern number, which for our model evaluates to -2 ($+2$) for the point node on the positive (negative) k_z axis [55]. However, class D does not yield a topological invariant for line nodes in high-symmetry planes. These rely on a lattice symmetry, namely on the twofold rotation axis along \hat{z} , which acts as

$$\tilde{\mathcal{P}} \mathcal{H}(-k_x, -k_y, k_z) \tilde{\mathcal{P}}^\dagger = \mathcal{H}(k_x, k_y, k_z), \quad (48)$$

with

$$\tilde{\mathcal{P}} = \begin{pmatrix} ie^{-i\pi J_z} & 0 \\ 0 & -ie^{i\pi J_z} \end{pmatrix}. \quad (49)$$

In the $k_x k_y$ plane, the twofold rotation maps $(k_x, k_y, 0)$ onto $(-k_x, -k_y, 0)$ and hence acts like spatial inversion. The product of charge conjugation \mathcal{C} and the pseudo-inversion $\tilde{\mathcal{P}}$ maps $(k_x, k_y, 0)$ onto itself and causes the spectrum to be symmetric for each momentum in the $k_x k_y$ plane. We further find that this product squares to $(\mathcal{C}\tilde{\mathcal{P}})^2 = +1$ since the antiunitary charge-conjugation operator reads $\mathcal{C} = U_C \mathcal{K}$ with $U_C = \tau_1 \otimes \mathbb{1}_4$, where τ_1 is a Pauli matrix in particle-hole space. Such a symmetry ensures that nodes of codimension 1 can have a \mathbb{Z}_2 topological invariant [56, 57]. In the two-dimensional $k_x k_y$ plane, line nodes can thus be topologically stable in the presence of a twofold rotation axis perpendicular to the plane. The method of Ref. [17] can be applied to construct this invariant in terms of a Pfaffian of $\mathcal{H}(k_x, k_y, 0)$.

The T_2 state of Eq. (47) is of particular relevance since there is experimental evidence for line nodes in YPtBi [24]. The other symmetry-allowed and energetically favorable E and T_2 pairing states do not have symmetry-protected line nodes for vanishing ASOC [25].

For the centrosymmetric variant with point group O_h , for which the ASOC is forbidden by symmetry, nodes of the superconducting gap are generically *inflated* into two-dimensional Bogoliubov Fermi surfaces for multiband pairing [17, 18]. In centrosymmetric multiband superconductors that spontaneously break time-reversal symmetry but satisfy $\mathcal{C}\mathcal{P}$ symmetry (the product of charge conjugation and inversion) squaring to $(\mathcal{C}\mathcal{P})^2 = +1$, nodal points and nodal lines are replaced by spheroidal and toroidal Bogoliubov Fermi surfaces, respectively. These Fermi surfaces are protected by a \mathbb{Z}_2 topological invariant, which can be expressed in terms of a Pfaffian [17, 18, 56, 57]. These results do not carry over to the present case since the T_d point group is not centrosymmetric and thus inversion and $\mathcal{C}\mathcal{P}$ symmetry are absent. The \mathbb{Z}_2 number [17, 18] cannot even be defined. Nevertheless, Bogoliubov Fermi surfaces can exist: Volovik [58] has pointed out that Fermi surfaces can appear in multiband systems if both inversion and time-reversal symmetry are broken and the interband pairing potential is sufficiently large. Examples of this are realized in Fulde-Ferrell [59] pairing states in single-band systems with Rashba spin-orbit coupling in an applied magnetic field [60], as well as in the proposed [61] coexistence state of d -wave superconductivity and loop-current order in $\text{YBa}_2\text{Cu}_3\text{O}_{7-\delta}$ [62]. Note that these proposals require both the inversion and the time-reversal-symmetry breaking to be extrinsic to the superconducting state; in contrast, in our system the time-reversal-symmetry breaking is intrinsic to the superconductivity.

The presence of Fermi surfaces in these systems can be understood as follows: due to the absence of $\mathcal{C}\mathcal{P}$ and $\mathcal{C}\mathcal{T}$ symmetries, the spectrum at fixed momentum \mathbf{k} is not symmetric. Hence, band crossings or avoided crossings generically do not occur at the Fermi energy and symmetry thus does not dictate any gap opening there. It is thus possible for bands to cross the Fermi energy. Since the band energies are continuous functions of momen-

tum, the crossings are generically two-dimensional Fermi surfaces. Of course, one expects that superconductivity is only energetically favorable if gaps do open at the Fermi energy, but this need not happen everywhere on the normal-state Fermi surface.

The nodal structure both for infinitesimal and finite pairing is best analyzed in terms of the determinant of the Bogoliubov-de Gennes Hamiltonian $\mathcal{H}(\mathbf{k})$ given in Eq. (19). The determinant is of course the product of the eigenenergies and thus its zeros coincide with the nodes. The determinant is expanded in the pairing amplitude $\Delta_{T_2}^0$, which is assumed to be real,

$$\det \mathcal{H}(\mathbf{k}) = \det \mathcal{H}(\mathbf{k})|_{\Delta=0} + g_2(\mathbf{k})(\Delta_{T_2}^0)^2 + g_4(\mathbf{k})(\Delta_{T_2}^0)^4. \quad (50)$$

This expansion is exact; higher orders do not occur since

$$\Delta(\mathbf{k}) = 4\Delta_{T_2}^0 \begin{pmatrix} 0 & 0 & 0 & 0 \\ 0 & 0 & 0 & i \\ 0 & 0 & 0 & 0 \\ 0 & -i & 0 & 0 \end{pmatrix} \quad (51)$$

so that the matrix $\mathcal{H}(\mathbf{k})$ only contains $\Delta_{T_2}^0$ linearly in four components. The determinant must be even in $\Delta_{T_2}^0$ due to invariance under global phase changes. The zero-order term in Eq. (50) is nonnegative since the spectrum is symmetric and contains an even number of pairs of eigenvalues. Hence, $\det \mathcal{H}(\mathbf{k})|_{\Delta=0}$ generically (not at the touching points) has second-order zeros forming a two-dimensional manifold, namely the Fermi surface.

The determinant $\det \mathcal{H}(\mathbf{k})$ of the full Hamiltonian is positive sufficiently far from the normal-state Fermi surface since superconductivity is then a small correction. A negative determinant at some momentum \mathbf{k} thus implies, using the continuity of the function $\mathbf{k} \mapsto \det \mathcal{H}(\mathbf{k})$, the existence of a Bogoliubov Fermi surface surrounding it. For small $\Delta_{T_2}^0$, this can only happen on the normal-state Fermi surface, where the zero-order term vanishes. To leading order, the existence of Fermi surfaces is determined by the coefficient $g_2(\mathbf{k}_F)$ on the Fermi surface. If $g_2(\mathbf{k}_F) > 0$ then the normal-state Fermi surface is gapped out in the vicinity of \mathbf{k}_F . For $g_2(\mathbf{k}_F) < 0$, there must be a Bogoliubov Fermi surface in the superconducting state. If $g_2(\mathbf{k}_F) = 0$ then it is necessary to go to higher orders.

It can be shown that $g_2(\mathbf{k}_F) \geq 0$ everywhere on the normal-state Fermi surface. Moreover, g_2 vanishes where the k_x , k_y , and k_z axes intersect the Fermi surfaces. The proof of these statements is given in the Appendix. Numerical results for g_2 on the Fermi surfaces are shown in Fig. 7. The plots show the nodal structure for infinitesimal pairing. Besides the zeros on the coordinate axes found rigorously, g_2 also vanishes along the equator of both surfaces and on additional nodal rings surrounding the coordinate axes only on the larger surface. These new nodal rings are reminiscent of the case of A_1 pairing in that they do not lie in high-symmetry planes. However, unlike for A_1 pairing, their size is controlled by the ASOC. Everywhere else, the coefficient g_2 is positive and the Fermi surface is gapped out in the superconducting

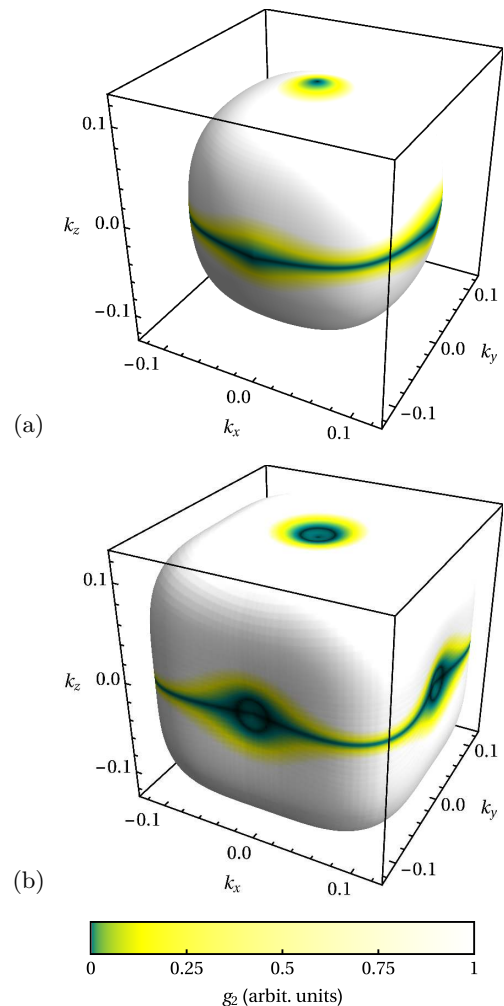


Figure 7. Coefficient g_2 in the expansion of $\det \mathcal{H}(\mathbf{k})$ in the pairing amplitude, Eq. (50), for the T_2 pairing state with order parameter $\mathbf{l} = (1, i, 0)$ on (a) the smaller and (b) the larger normal-state Fermi surface. The plots exhibit the nodal structure for infinitesimal pairing.

state. Hence, for infinitesimal pairing, the point and line nodes of the single-band T_2 state survive but we obtain additional nodal rings on one of the Fermi surfaces.

If the pairing amplitude is not infinitesimal, we have to go beyond second order in $\Delta_{T_2}^0$. However, using Eq. (50) is inconvenient since the minima of $\det \mathcal{H}(\mathbf{k})$ generically occur off the Fermi surface, necessitating a double expansion in the pairing amplitude and the deviation of \mathbf{k} normal to the Fermi surface. Instead, we have numerically examined $\det \mathcal{H}(\mathbf{k})$. The results for $\Delta_{T_2}^0 = 3 \text{ meV}$ are shown in Fig. 8.

In more detail, we find the following results: (i) The two line nodes along the equators survive but the breaking of time-reversal symmetry splits their touching points on the k_x and k_y axes. (ii) In the vicinity of these points, regions with $\det \mathcal{H}(\mathbf{k}) < 0$ emerge, where the number of bands below (and above) the Fermi energy

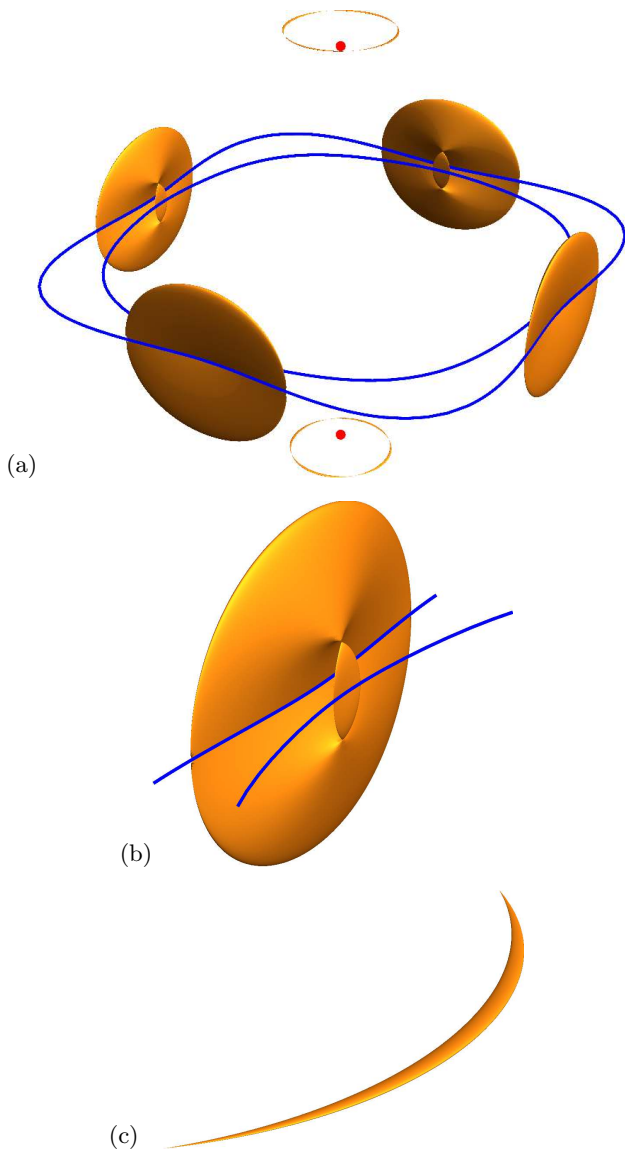


Figure 8. (a) Nodes for the T_2 pairing state with order parameter $\mathbf{l} = (1, i, 0)$, which breaks time-reversal symmetry, and pairing amplitude $\Delta_{T_2}^0 = 3 \text{ meV}$. Red dots represent point nodes, blue lines line nodes, and orange surfaces Bogoliubov Fermi surfaces. Momentum axes are omitted for clarity. Note, however, that the point nodes coincide with the ones in Fig. 7. (b) Enlargement of the system of Fermi pockets and line nodes close to the k_x and k_y axes. (c) Enlargement of one of the sickle-shaped Fermi pockets close to the point nodes.

is odd. These regions are bounded by two-dimensional Bogoliubov Fermi surfaces (inflated nodes) of complex shape. Figure 8(b) shows an enlarged view of one set of these pockets, consisting of a large plate-like pocket and a smaller pocket that touches the larger one at two points. The surface of each of the two pockets crosses itself at one of the nodal lines. The pockets evolve from the additional nodal rings around the k_x and k_y axes in Fig.

7(b), which are inflated for growing $\Delta_{T_2}^0$, and transform into the shapes in Fig. 8(b) through a series of Lifshitz transitions. (iii) There are still two point nodes on the k_z axis. The quasiparticle dispersion close to these nodes is linear in the k_z direction but quadratic in the two orthogonal directions. The point nodes have Chern numbers of ± 2 [55]. (iv) The nodal rings surrounding the k_z axis on the larger Fermi surface, see Fig. 7(b), are inflated into Bogoliubov Fermi surfaces with four pinch points for $|k_x| = |k_y|$, resulting in four sickle-shaped pockets for each ring. An enlargement of one of these pockets is shown in Fig. 8(c).

It is worth emphasizing that point and line nodes coexist with Bogoliubov Fermi pockets. As discussed above, point nodes protected by an integer Chern number are allowed for class D, while line nodes are protected by class D in conjunction with a twofold rotation symmetry. Neither the multiband character nor the breaking of inversion symmetry by the ASOC affect these symmetries. The point nodes inherit the Chern numbers ± 2 from the inversion-symmetric, weak pairing limit. Since the model stays in class D when multiband pairing and ASOC are switched on, these topological invariants could only vanish by merging in the $k_x k_y$ plane. However, generically the point nodes can split into two each with Chern numbers ± 1 . We find that this splitting is disallowed by the combination of charge-conjugation symmetry and four-fold rotoinversion symmetry about the z -axis. On the other hand, the Bogoliubov Fermi pockets are not topologically protected. As noted above, bands crossing the Fermi energy are allowed by the breaking of time-reversal symmetry, which generically makes avoided band crossings happen away from the Fermi energy.

2. Surface states

Figure 9 shows the dispersion of surface states at the (111) and (100) surfaces. Note that for the T_2 pairing state, (100) is not equivalent to (001). Outside of the projection of the normal-state Fermi surface, we again find weakly modified descendants of the normal surface states shown in Fig. 3. Also visible are the projections of the inflated nodes allowed by the broken time-reversal symmetry. There are no flat bands associated with the line nodes in the high-symmetry plane. Flat bands are not expected since the line nodes are not protected by a winding number [63], unlike the line nodes in the A_1 state, but by a \mathbb{Z}_2 invariant that only exists in the $k_x k_y$ plane. Hence, this \mathbb{Z}_2 number does not induce a global invariant on gapped one-dimensional subsystems and one cannot construct an argument for flat bands in analogy to the A_1 case. There are also no flat bands from the inflated nodal rings that are not lying in the symmetry plane, i.e., the small orange rings at the top and bottom of Fig. 8(a). Their projections are visible in Fig. 9(a) as two ellipses that cross the $k_1 = 0$ line and intersect the projections of the outer nodal line in the symmetry

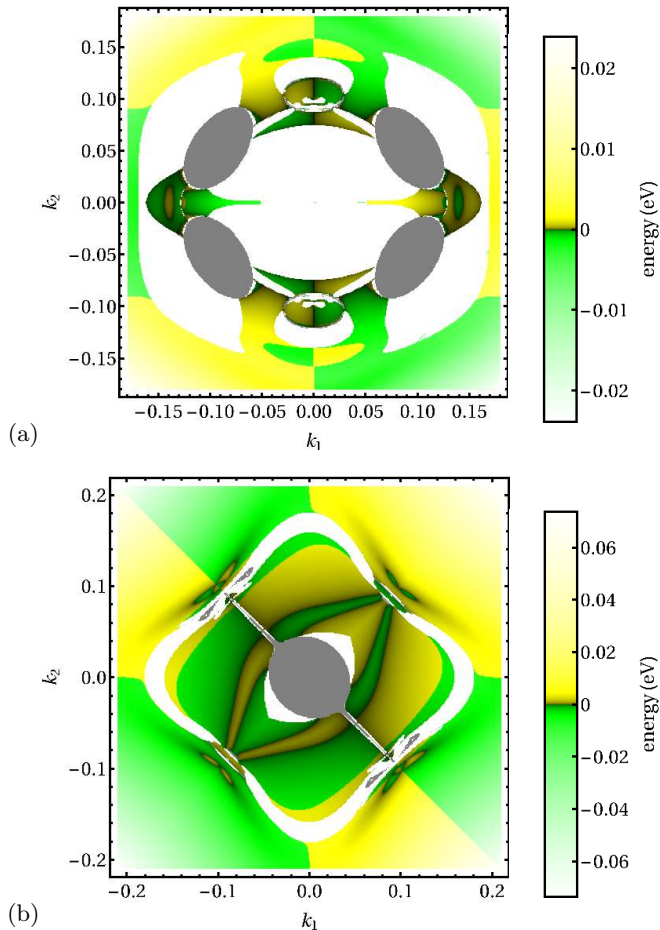


Figure 9. Dispersion of surface states of YPtBi in the superconducting T_2 state for (a) the (111) surface with a thickness of $W = 16000$ and (b) the (100) surface with $W = 4000$. A larger thickness was considered for the (111) surface because of large finite-size effects. The spectra at fixed momentum are not symmetric. The signful energy closest to the Fermi energy is plotted. The gray regions are the projections of the Bogoliubov Fermi pockets shown in Fig. 8 onto the surface Brillouin zone. In these regions, states exist at the Fermi energy and are bulk like. In the white regions, there are no Fermi pockets but the states closest to the Fermi energy are still bulk like.

plane. We conclude that these inflated rings are also not protected by a winding number.

Furthermore, we observe dispersive surface states where the normal-state Fermi sea has been gapped out. Their dispersion crosses the Fermi energy at arclike lines emanating from the projections of the point nodes for both the (111) and the (100) slab. These arcs show up as black lines separating yellow and green regions in Figs. 9(a) and 9(b). For the (111) slab, Fig. 9(a), the projections of the point nodes lie within the projections of the inflated rings. Two arcs start from each point node, consistent with its Chern number ± 2 . One arc, which is clearly visible, connects to the inflated ring. The other

connects to the projection of the outer ring in the $k_x k_y$ plane and is obscured by bulk states (white region). The arcs are straight lines lying in the projection of a mirror plane, cf. Sec. III A. Due to the mirror symmetry, the spectrum and in particular the arcs are twofold degenerate. Correcting for the double counting in the Nambu formalism, this corresponds to a single arc; a single pair of helical Majorana bands crosses here. For the (100) slab, Fig. 9(b), four arcs are associated with each point node, where the point nodes themselves are obscured by bulk states. The appearance of four arcs instead of two can be understood as follows: The centrosymmetric variant of the model has a symmetric spectrum at each \mathbf{k}_{\parallel} and thus wherever a Majorana surface band with dispersion $E(\mathbf{k}_{\parallel})$ crosses the Fermi energy, forming an arc, another band with dispersion $-E(\mathbf{k}_{\parallel})$ also crosses the Fermi energy. In the present case the centrosymmetric variant has two arcs associated with each point node. The simultaneous breaking of inversion and time-reversal symmetry shifts this crossing to finite energy and thus splits each arc into two. This is consistent with the observation that neighboring arcs in Fig. 9(b) have opposite velocities. The crossing of the surface bands happens between these arcs.

IV. SUMMARY AND CONCLUSIONS

Bulk and surface states of two plausible superconducting states of half-Heusler compounds have been analyzed, taking YPtBi as a specific example. Their partially filled Γ_8 band is described in terms of the effective angular momentum $j = 3/2$. The inverted band structure of YPtBi and several other half-Heusler compounds [26–28] leads to the appearance of surface states of topological origin even in the normal phase. These compounds are also noncentrosymmetric and thus allow us to study the fate of characteristic properties of noncentrosymmetric superconductors, such as flat surface bands, in a multi-band system. YPtBi is a particularly promising candidate for topological superconductivity based on experimental reports of a zero-bias peak in tunneling [24], which hints at such flat surface bands. Technically, we have performed numerical diagonalization of Bogoliubov-de Gennes Hamiltonians for slabs with (111) and (100) oriented surfaces.

We consider a A_1 pairing state that leaves time-reversal symmetry intact and a T_2 pairing state that breaks time-reversal and also lattice symmetries. The two states have in common that they allow for line nodes of the superconducting gap, which are supported by measurements of the London penetration depth [24].

For the A_1 state, the line nodes require the symmetry-allowed admixture of nonlocal p -wave pairing [25]. The A_1 state has six nodal rings surrounding the cubic coordinate axes. The nodal rings are associated with nonzero winding numbers ± 1 . These protect flat zero-energy surface bands bounded by the projections of a *single* nodal

ring onto the surface Brillouin zone. Such flat bands have been found for single-band noncentrosymmetric models [14, 15, 21, 22, 47, 48]. We here find that they persist in the multiband case, in particular, they are not gapped out by interband pairing. On the other hand, the multiband character allows for additional pairing states that are not possible for single-band superconductors. The A_1 state considered here is a superposition of singlet ($J = 0$) and septet ($J = 3$) pairing, where the latter is possible because of the effective spin $j = 3/2$ of the electrons. In addition, we have obtained dispersive surface states. They are in part derived from the normal-phase surface states, but interesting new effects emerge where the normal-phase Fermi sea is gapped out by superconductivity. Here, Fermi arcs appear when mirror planes are perpendicular to the surface. They are restricted to the projection of the mirror plane onto the surface Brillouin zone and are protected by a mirror parity.

The time-reversal-symmetry-breaking T_2 state has interesting nodal structure already in the bulk. Even for infinitesimal pairing, the ASOC changes the nodal structure compared to the centrosymmetric variant of the model or the case of vanishing ASOC [25]: besides point nodes generic for topological superconductors in class D and line nodes in a high-symmetry plane, which rely on a twofold rotation axis, the system has additional nodal rings, reminiscent of the A_1 case. If the pairing amplitude is not infinitesimal we find that the point nodes and the line nodes in the high-symmetry plane survive but now coexist with two-dimensional Bogoliubov Fermi pockets (inflated nodes). At surfaces, the T_2 superconductor does not show flat bands, due to the lack of winding numbers that could protect them. There are dispersive surface states with Fermi arcs associated with projections of the point nodes. The arcs for the (100) surface are split due to the absence of time-reversal and inversion symmetry so that their number is doubled compared to systems with time-reversal or inversion symmetry and the same Chern numbers of the point nodes. For the (111) surface, the arcs lie in a mirror plane, which prevents the splitting.

Note added: Recently, a preprint by Yang *et al.* [64] appeared that also addresses the flat-band surface states for A_1 pairing.

ACKNOWLEDGMENTS

The authors thank J. Paglione, H. Kim, and H. Nakamura for stimulating discussions. C. T. acknowledges financial support by the Deutsche Forschungsgemeinschaft, in part through Research Training Group GRK 1621 and Collaborative Research Center SFB 1143. D. A. acknowledges support from the National Science Foundation Grant No. DMREF-1335215 and the hospitality of the Pauli Center of the ETH Zürich. P. M. R. B. acknowledges the hospitality of the TU Dresden.

Appendix A: Expansion of the determinant of the Bogolibov-de Gennes Hamiltonian

We here show that the coefficient

$$g_2 = \frac{1}{2} \frac{d^2}{d\Delta^2} \det \mathcal{H} \Big|_{\Delta=0} \quad (\text{A1})$$

in the expansion (50) is nonnegative everywhere on the Fermi surface and is zero where the cubic axes intersect the Fermi surface. The short-hand notation $\Delta = \Delta_{T_2}^0$ is used and the momentum argument is suppressed.

Take E to be a real energy but not an eigenvalue of $\mathcal{H}(\mathbf{k})$. Then $\mathcal{H}(\mathbf{k}) - E$ is invertable (an identity matrix is suppressed) and we have

$$\frac{d}{d\Delta} \det(\mathcal{H} - E) = \det(\mathcal{H} - E) \text{Tr}(\mathcal{H} - E)^{-1} \frac{d\mathcal{H}}{d\Delta} \quad (\text{A2})$$

and

$$\begin{aligned} \frac{d^2}{d\Delta^2} \det(\mathcal{H} - E) &= \det(\mathcal{H} - E) \left[\text{Tr}(\mathcal{H} - E)^{-1} \frac{d\mathcal{H}}{d\Delta} \right]^2 \\ &\quad - \det(\mathcal{H} - E) \text{Tr}(\mathcal{H} - E)^{-1} \frac{d\mathcal{H}}{d\Delta} (\mathcal{H} - E)^{-1} \frac{d\mathcal{H}}{d\Delta}. \end{aligned} \quad (\text{A3})$$

Note that

$$\frac{d\mathcal{H}}{d\Delta} = 4 \left(\begin{array}{ccc|ccc} & & & 0 & 0 & 0 & 0 \\ & & & 0 & 0 & 0 & i \\ & & & 0 & 0 & 0 & 0 \\ & & & 0 & -i & 0 & 0 \\ \hline 0 & 0 & 0 & 0 & & & \\ 0 & 0 & 0 & i & & & \\ 0 & 0 & 0 & 0 & & & 0 \\ 0 & -i & 0 & 0 & & & \end{array} \right). \quad (\text{A4})$$

Setting $\Delta = 0$ we thus get

$$\begin{aligned} \frac{d}{d\Delta} \det(\mathcal{H} - E) \Big|_{\Delta=0} &= \text{Tr} \left(\begin{array}{cc} h - E & 0 \\ 0 & -h^T - E \end{array} \right)^{-1} \frac{d\mathcal{H}}{d\Delta} \\ &= \text{Tr} \left(\begin{array}{cc} (h - E)^{-1} & 0 \\ 0 & (-h^T - E)^{-1} \end{array} \right) \frac{d\mathcal{H}}{d\Delta} = 0 \end{aligned} \quad (\text{A5})$$

and, using this,

$$\begin{aligned} \frac{d^2}{d\Delta^2} \det(\mathcal{H} - E) \Big|_{\Delta=0} &= -\det(\mathcal{H} - E) \\ &\quad \times \text{Tr}(\mathcal{H} - E)^{-1} \frac{d\mathcal{H}}{d\Delta} (\mathcal{H} - E)^{-1} \frac{d\mathcal{H}}{d\Delta} \Big|_{\Delta=0}. \end{aligned} \quad (\text{A6})$$

We denote the eigenvalues and eigenvectors of \mathcal{H} for $\Delta = 0$ by E_i and $|i\rangle$, respectively. The spectrum is symmetric; we enumerate the eigenvalues in such a way that $E_{-i} = -E_i$. Then

$$\begin{aligned} \frac{d^2}{d\Delta^2} \det(\mathcal{H} - E) \Big|_{\Delta=0} &= -\prod_k (E_k - E) \\ &\quad \times \sum_{ij} \frac{|\langle i | d\mathcal{H}/d\Delta | j \rangle|^2}{(E_i - E)(E_j - E)}. \end{aligned} \quad (\text{A7})$$

Now take \mathbf{k} on the normal-state Fermi surface. There are two cases: The corresponding normal-state eigenvalue can be nondegenerate or twofold degenerate. The latter happens at the intersection of the Fermi surface with the cubic axes.

Case 1: nondegenerate eigenvalue. We take $E_1 = E_{-1} = 0$ and write

$$\prod_k (E_k - E) = E^2 \prod_{k \neq \pm 1} (E_k - E). \quad (\text{A8})$$

In the sum over i, j , the terms with $i, j \in \{1, -1\}$ have the denominator E^2 , which cancels with the E^2 in the prefactor. The terms with only one of i or j from $\{1, -1\}$ contain only one factor E in the denominator, with leaves an overall factor of E . The terms with $i, j \notin \{1, -1\}$ retain a prefactor of E^2 . We now take the limit $E \rightarrow 0$, i.e., E goes to the Fermi energy. Only the first term survives so that

$$g_2 = \frac{1}{2} \frac{d^2}{d\Delta^2} \det \mathcal{H} \Big|_{\Delta=0} = -\frac{1}{2} \prod_{k \neq \pm 1} E_k \sum_{i, j = \pm 1} \left| \langle i | \frac{d\mathcal{H}}{d\Delta} | j \rangle \right|^2. \quad (\text{A9})$$

Using that the spectrum is symmetric, this yields

$$g_2 = \frac{1}{2} E_2^2 E_3^2 E_4^2 \sum_{i, j = \pm 1} \left| \langle i | \frac{d\mathcal{H}}{d\Delta} | j \rangle \right|^2 \geq 0. \quad (\text{A10})$$

Case 2: degenerate eigenvalue. We take $E_{\pm 1} = E_{\pm 2} = 0$ and write

$$\prod_k (E_k - E) = E^4 \prod_{k \neq \pm 1, \pm 2} (E_k - E). \quad (\text{A11})$$

The terms in the sum over i, j in Eq. (A7) are at most of order $1/E^2$ for small E . Hence, all terms vanish in the limit $E \rightarrow 0$ and we obtain $g_2 = 0$.

-
- [1] C. Nayak, S. H. Simon, A. Stern, M. Freedman, and S. Das Sarma, nonAbelian anyons and topological quantum computation, *Rev. Mod. Phys.* **80**, 1083 (2008).
- [2] J. Aliceak, New directions in the pursuit of Majorana fermions in solid state systems, *Rep. Prog. Phys.* **75**, 076501 (2012).
- [3] C. W. J. Beenakker, Search for Majorana Fermions in Superconductors, *Ann. Rev. Condens. Matter Phys.* **4**, 113 (2013).
- [4] T. D. Stanescu and S. Tewari, Majorana fermions in semiconductor nanowires: fundamentals, modeling, and experiment, *J. Phys.: Condens. Matter* **25**, 233201 (2013).
- [5] S. Nadj-Perge, I. K. Drozdov, J. Li, H. Chen, S. Jeon, J. Seo, A. H. MacDonald, B. A. Bernevig, A. Yazdani, Observation of Majorana fermions in ferromagnetic atomic chains on a superconductor, *Science* **346**, 602 (2014).
- [6] A. P. Schnyder, S. Ryu, A. Furusaki, and A. W. W. Ludwig, Classification of topological insulators and superconductors in three spatial dimensions, *Phys. Rev. B* **78**, 195125 (2008); Classification of Topological Insulators and Superconductors, *AIP Conf. Proc.* **1134**, 10 (2009).
- [7] A. Kitaev, Periodic table for topological insulators and superconductors, *AIP Conf. Proc.* **1134**, 22 (2009).
- [8] M. R. Zirnbauer, Riemannian symmetric superspaces and their origin in random-matrix theory, *J. Math. Phys. (N.Y.)* **37**, 4986 (1996); A. Altland and M. R. Zirnbauer, Nonstandard symmetry classes in mesoscopic normal-superconducting hybrid structures, *Phys. Rev. B* **55**, 1142 (1997).
- [9] S. Ryu and Y. Hatsugai, Topological Origin of Zero-Energy Edge States in Particle-Hole Symmetric Systems, *Phys. Rev. Lett.* **89**, 077002 (2002).
- [10] G. E. Volovik, *Universe in a Helium Droplet* (Oxford University Press, Oxford, 2003).
- [11] Y. Tanaka, Y. Mizuno, T. Yokoyama, K. Yada, and M. Sato, Anomalous Andreev Bound State in Noncentrosymmetric Superconductors, *Phys. Rev. Lett.* **105**, 097002 (2010); K. Yada, M. Sato, Y. Tanaka, and T. Yokoyama, Surface density of states and topological edge states in noncentrosymmetric superconductors, *Phys. Rev. B* **83**, 064505 (2011).
- [12] M. Sato, Y. Tanaka, K. Yada, and T. Yokoyama, Topology of Andreev bound states with flat dispersion, *Phys. Rev. B* **83**, 224511 (2011).
- [13] G. E. Volovik, Flat band in the core of topological defects: Bulk-vortex correspondence in topological superfluids with Fermi points, *JETP Lett.* **93**, 66 (2011).
- [14] P. M. R. Brydon, A. P. Schnyder, and C. Timm, Topologically protected flat zero-energy surface bands in noncentrosymmetric superconductors, *Phys. Rev. B* **84**, 020501(R) (2011).
- [15] A. P. Schnyder and S. Ryu, Topological phases and surface flat bands in superconductors without inversion symmetry, *Phys. Rev. B* **84**, 060504(R) (2011).
- [16] C.-K. Chiu, J. C. Y. Teo, A. P. Schnyder, and S. Ryu, Classification of topological quantum matter with symmetries, *Rev. Mod. Phys.* **88**, 035005 (2016).
- [17] D. F. Agterberg, P. M. R. Brydon, and C. Timm, Bogoliubov Fermi Surfaces in Superconductors with Broken Time-Reversal Symmetry, *Phys. Rev. Lett.* **118**, 127001 (2017).
- [18] T. Bzdušek and M. Sigrist, Robust and multiply charged nodes in centrosymmetric systems, arXiv:1705.07126.
- [19] E. Bauer and M. Sigrist, *noncentrosymmetric Superconductors—Introduction and Overview* (Springer, New York, 2012).

- [20] M. Smidman, M. B. Salamon, H. Q. Yuan, and D. F. Agterberg, Superconductivity and spin-orbit coupling in noncentrosymmetric materials: a review, *Rep. Prog. Phys.* **80**, 036501 (2017).
- [21] A. P. Schnyder, P. M. R. Brydon, and C. Timm, Types of topological surface states in nodal noncentrosymmetric superconductors, *Phys. Rev. B* **85**, 024522 (2012).
- [22] A. P. Schnyder and P. M. R. Brydon, Topological surface states in nodal superconductors, *J. Phys.: Condens. Matter* **27**, 243201 (2015).
- [23] T. V. Bay, T. Naka, Y. K. Huang, and A. de Visser, Superconductivity in noncentrosymmetric YPtBi under pressure, *Phys. Rev. B* **86**, 064515 (2012).
- [24] H. Kim, K. Wang, Y. Nakajima, R. Hu, S. Ziemak, P. Syers, L. Wang, H. Hodovanets, J. D. Denlinger, P. M. R. Brydon, D. F. Agterberg, M. A. Tanatar, R. Prozorov, and J. Paglione, Beyond Triplet: Unconventional Superconductivity in a Spin-3/2 Topological Semimetal, arXiv:1603.03375.
- [25] P. M. R. Brydon, L. M. Wang, M. Weinert, and D. F. Agterberg, Pairing of $j = 3/2$ Fermions in Half-Heusler Superconductors, *Phys. Rev. Lett.* **116**, 177001 (2016).
- [26] S. Chadov, X. Qi, J. Kübler, G. H. Fecher, C. Felser, and S. C. Zhang, Tunable multifunctional topological insulators in ternary Heusler compounds, *Nat. Mater.* **9**, 541 (2010).
- [27] H. Lin, L. A. Wray, Y. Xia, S. Xu, S. Jia, R. J. Cava, A. Bansil, and M. Z. Hasan, Half-Heusler ternary compounds as new multifunctional experimental platforms for topological quantum phenomena, *Nat. Mater.* **9**, 546 (2010).
- [28] Z. K. Liu, L. X. Yang, S.-C. Wu, C. Shekhar, J. Jiang, H. F. Yang, Y. Zhang, S.-K. Mo, Z. Hussain, B. Yan, C. Felser, and Y. L. Chen, Observation of unusual topological surface states in half-Heusler compounds LnPtBi (Ln=Lu, Y), *Nat. Commun.* **7**, 12924 (2016).
- [29] N. P. Butch, P. Syers, K. Kirshenbaum, A. P. Hope, and J. Paglione, Superconductivity in the topological semimetal YPtBi, *Phys. Rev. B* **84**, 220504(R) (2011).
- [30] F. F. Tafti, T. Fujii, A. Juneau-Fecteau, S. R. de Cotret, N. Doiron-Leyraud, A. Asamitsu, and L. Taillefer, Superconductivity in the noncentrosymmetric half-Heusler compound LuPtBi: A candidate for topological superconductivity, *Phys. Rev. B* **87**, 184504 (2013).
- [31] C. Fang, B. A. Bernevig, and M. J. Gilbert, Tri-Dirac surface modes in topological superconductors, *Phys. Rev. B* **91**, 165421 (2015).
- [32] W. Yang, Y. Li, and C. Wu, Topological Septet Pairing with Spin-3/2 Fermions: High-Partial-Wave Channel Counterpart of the $^3\text{He-B}$ Phase, *Phys. Rev. Lett.* **117**, 075301 (2016).
- [33] I. Boettcher and I. F. Herbut, Unconventional Superconductivity in Luttinger Semimetals: Theory of Complex Tensor Order and Emergence of the Uniaxial Nematic State, arXiv:1707.03444.
- [34] L. Savary, J. Ruhman, J. W. F. Venderbos, L. Fu, and P. A. Lee, Superconductivity in three-dimensional spin-orbit coupled semimetals, arXiv:1707.03831.
- [35] M. Kharitonov, J.-B. Mayer, and E. M. Hankiewicz, Universality and stability of the edge states of chiral nodal topological semimetals; Luttinger model for $j = 3/2$ electrons as a 3D topological semimetal, arXiv:1701.01553.
- [36] M. Meinert, Unconventional Superconductivity in YPtBi and Related Topological Semimetals, *Phys. Rev. Lett.* **116**, 137001 (2016).
- [37] G. Racah, Theory of Complex Spectra. II, *Phys. Rev.* **62**, 438 (1942).
- [38] K. W. H. Stevens, Matrix Elements and Operator Equivalents Connected with the Magnetic Properties of Rare Earth Ions, *Proc. Phys. Soc.* **A65**, 209 (1952).
- [39] O. Danielsen and P.-A. Lindgård, *Quantum mechanical operator equivalents used in the theory of magnetism*, Risø Report No. 259 (Forskningssenter Risø, 1972).
- [40] M. Sato, Nodal structure of superconductors with time-reversal invariance and Z_2 topological number, *Phys. Rev. B* **73**, 214502 (2006); M. Sato and S. Fujimoto, Topological phases of noncentrosymmetric superconductors: Edge states, Majorana fermions, and nonAbelian statistics, *ibid.* **79**, 094504 (2009).
- [41] B. Béri, Topologically stable gapless phases of time-reversal-invariant superconductors, *Phys. Rev. B* **81**, 134515 (2010).
- [42] P. A. Frigeri, D. F. Agterberg, A. Koga, and M. Sigrist, Superconductivity without Inversion Symmetry: MnSi versus CePt₃Si, *Phys. Rev. Lett.* **92**, 097001 (2004).
- [43] F. Tran and P. Blaha, Accurate Band Gaps of Semiconductors and Insulators with a Semilocal Exchange-Correlation Potential, *Phys. Rev. Lett.* **102**, 226401 (2009).
- [44] M. I. D'yakonov and A. V. Khaetskii, Surface states in a gapless semiconductor, *JETP Lett.* **33**, 110 (1981).
- [45] R.-L. Chu, W.-Y. Shan, J. Lu, and S.-Q. Shen, Surface and edge states in topological semimetals, *Phys. Rev. B* **83**, 075110 (2011).
- [46] A. Lau and C. Timm, Topological surface states in paramagnetic and antiferromagnetic iron pnictides, *Phys. Rev. B* **88**, 165402 (2013); Topological surface states and Andreev bound states in superconducting iron pnictides, *ibid.* **90**, 024517 (2014).
- [47] P. M. R. Brydon, C. Timm, and A. P. Schnyder, Interface currents in topological superconductor-ferromagnet heterostructures, *New J. Phys.* **15**, 045019 (2013).
- [48] A. P. Schnyder, C. Timm, and P. M. R. Brydon, Edge Currents as a Signature of Flatbands in Topological Superconductors, *Phys. Rev. Lett.* **111**, 077001 (2013).
- [49] P. M. R. Brydon, A. P. Schnyder, and C. Timm, Helical spin texture of surface states in topological superconductors, *New J. Phys.* **17**, 013016 (2015).
- [50] M. Abolfath, T. Jungwirth, J. Brum, and A. H. MacDonald, Theory of magnetic anisotropy in $\text{III}_{1-x}\text{Mn}_x\text{V}$ ferromagnets, *Phys. Rev. B* **63**, 054418 (2001).
- [51] T. Jungwirth, J. Sinova, J. Mašek, J. Kučera, and A. H. MacDonald, Theory of ferromagnetic (III,Mn)V semiconductors, *Rev. Mod. Phys.* **78**, 809 (2006).
- [52] Note that the relation would be different if the four-dimensional Hilbert space at fixed \mathbf{k} results from the combination of two spin-full orbitals of the same parity, as discussed in the Supplemental Material of Ref. [17]. Operators would then be expressed in terms of Kronecker products $s_\mu \otimes \sigma_\nu$, $\mu, \nu = 0, x, y, z$ of identity and Pauli matrices s_μ in orbital space and σ_ν in spin space, respectively. The mapping to the effective-spin-3/2 basis [17] can then be used to find the spin-1/2 operators in the effective $J = 3/2$ representation.
- [53] M. Sigrist and K. Ueda, Phenomenological theory of unconventional superconductivity, *Rev. Mod. Phys.* **63**, 239 (1991).
- [54] C.-K. Chiu and A. P. Schnyder, Classification of re-

- flection-symmetry-protected topological semimetals and nodal superconductors, Phys. Rev. B **90**, 205136 (2014).
- [55] The Chern number ± 2 is obtained by taking the Bogoliubov-de Gennes Hamiltonian literally, which agrees with the convention used in Ref. [18]. A different convention is used in Ref. [22], which corresponds to dividing the Chern number by 2 to account for the double counting of degrees of freedom in the Nambu formalism. These different conventions also lead to conflicting meanings of the term “double Weyl point” in these papers.
- [56] S. Kobayashi, K. Shiozaki, Y. Tanaka, and M. Sato, Topological Blount’s theorem of odd-parity superconductors, Phys. Rev. B **90**, 024516 (2014).
- [57] Y. X. Zhao, A. P. Schnyder, and Z. D. Wang, Unified Theory of PT and CP Invariant Topological Metals and Nodal Superconductors, Phys. Rev. Lett. **116**, 156402 (2016).
- [58] G. E. Volovik, Zeroes in energy gap in superconductors with high transition temperature, Phys. Lett. A **142**, 282 (1989).
- [59] P. Fulde and R. A. Ferrell, Superconductivity in a Strong Spin-Exchange Field, Phys. Rev. **135**, A550 (1964).
- [60] Y. Xu, F. Zhang, and C. Zhang, Structured Weyl Points in Spin-Orbit Coupled Fermionic Superfluids, Phys. Rev. Lett. **115**, 265304 (2015).
- [61] C. M. Varma, non-Fermi-liquid states and pairing instability of a general model of copper oxide metals, Phys. Rev. B **55**, 14554 (1997); Pseudogap Phase and the Quantum-Critical Point in Copper-Oxide Metals, Phys. Rev. Lett. **83**, 3538 (1999).
- [62] L. Wang and O. Vafek, Quantum oscillations of the specific heat in d-wave superconductors with loop current order, Phys. Rev. B **88**, 024506 (2013)
- [63] S. Kobayashi, Y. Tanaka, and M. Sato, Fragile surface zero-energy flat bands in three-dimensional chiral superconductors, Phys. Rev. B **92**, 214514 (2015).
- [64] W. Yang, T. Xiang, and C. Wu, Majorana surface modes of nodal topological pairings in spin- $\frac{2}{3}$ semimetals, arXiv:1707.07261.